Thin Solid Films 550 (2014) 575–581

Contents lists available at ScienceDirect

Thin Solid Films

journal homepage: www.elsevier.com/locate/tsf

Flash light sintering of nickel nanoparticles for printed electronics

Sung-Hyeon Park [a], Hak-Sung Kim [a,b]

[a] School of Mechanical Engineering, Hanyang University, 17 Haengdang-dong, Seongdong-gu, Seoul 133-791, Republic of Korea
[b] Institute of Nano Science and Technology, Hanyang University, Seoul 133-79, Republic of Korea

ARTICLE INFO

Article history:
Received 12 February 2013
Received in revised form 15 November 2013
Accepted 15 November 2013
Available online 23 November 2013

Keywords:
Printed electronic
Multilayer ceramic capacitors
Nickel
Flash light
Sintering
Nanoparticle
Size effect

ABSTRACT

In this paper, a sintering process for nickel nanoparticles using flash light irradiation was investigated for multilayer ceramic capacitors, magnetic devices and printed electronics. The existence of a small amount of 10 nm size nanoparticles in the ink significantly improved the flash light absorption and induced the melting and sintering of the nanoparticles. Due to this phenomenon, uniform diameter nickel nanoparticles (50 nm) could not be sintered, while the nickel nanoparticles with varying diameters (5–500 nm) were sintered by flash light irradiation.

In order to acquire high electrical conductivity in the sintered nickel nanoparticles, several flash light sintering parameters such as light energy and pulsed light patterns were optimized. Also, the nickel nano-ink was optimized by changing the weight fractions of organic binder in the ink.

1. Introduction

Nickel has been used extensively in various applications, including multilayer ceramic capacitors (MLCCs), magnetic devices and electrodes for supercapacitors in the electronics industry [1–13]. In MLCCs, the development of base-metal electrodes (BMEs) played an important role in expanding the potential applications. For BME applications, nickel electrodes recently attracted a lot of attention as they can reduce fabrication cost at least 10-fold compared to materials conventionally used for BME inner electrodes such as palladium and gold [1–5].

In magnetic devices, transition metal magnetic nanoparticles such as Fe, Co and Ni are widely used owing to their ferromagnetic properties. Also, these materials have been studied extensively because of their size- and shape-dependent physical, chemical and magnetic properties. Among these, nickel nanoparticles are mainly used due to their low cost and favorable melting temperature [6–9].

Recently, printed electronics have been studied as an alternative to the conventional photolithography process for electronic devices as printing offers many advantages such as substrate flexibility, low cost and ease of processing [10]. Most researchers have used gold and silver nanoparticles to fabricate electrical circuits due to their low melting temperature, low electrical resistivity, and thermodynamic stability (no oxidation phenomenon) [10–13]. However, the cost of silver and gold are about $17 and $1100 per ounce, while the cost of copper and nickel are about 20 cents and 53 cents per ounce, respectively [11]. Unfortunately, copper and nickel nanoparticles are easily oxidized upon contact with air. This makes the sintering process very complicated as an inert or reductive gas must be supplied to prevent oxidation or to reduce the oxide layers and transform them to a pure metal. Therefore, in our previous studies, we proposed a flash light sintering method to overcome the problems of thermal sintering methods [12–15]. The flash light sintering method has merit in that the process is carried out at room temperature under ambient conditions at ultra-fast speed (~ms). In the sintering of copper nanoparticles, the flash light irradiation was shown to reduce the copper oxide shell and transform it to pure copper when used in combination with a poly(N-vinylpyrrolidone) polymer coating on the copper nanoparticles [12]. In a separate work, in-situ reactive reducing and sintering of copper nanoparticles at room temperature and ambient conditions was demonstrated [14]. Furthermore, flash light sintering can prevent damage to various flexible substrates that may have a low melting or glass transition temperatures such as polyethylene and polyethylene terephthalate [14]. Light-assisted sintering of metal particles has been employed by several researchers. The summary of these studies are shown in Table 1. However, a study of the flash light sintering of nickel nanoparticles has not been conducted yet.

As mentioned above, the sintering of nickel nanoparticles is crucial for fabrication of MLCCs, magnetic devices, and printed electronics. However, sintering of nickel nanoparticles by a thermal sintering method is impossible without an inert or reducing gas chamber due to the fact that the melting temperature (300–600 °C) is higher than the oxidation temperature (135 °C); as such, nickel nanoparticles oxidize prior to melting or sintering [3,4,29]. The flash light sintering method mentioned above would be a promising alternative to alleviate these problems.

Therefore, in this work, we investigated the flash light sintering process for nickel nanoparticles. Specifically, we investigated the effect of

E-mail address: kima@hanyang.ac.kr (H.-S. Kim).

0040-6090/$ – see front matter
http://dx.doi.org/10.1016/j.tsf.2013.11.075

Table 1
The summary of the reported light-assisted sintering with respect to applied metal, light source, substrate, and conductivity.

Metal	Light source	Substrate	Conductivity	Author
Silver	Infrared ray (IR)	Glass	3 μΩ cm	Tobjörk [16]
		Paper	6 μΩ cm	
Silver	Flash light	Glass	24 μΩ cm	Galagan [17]
Silver	Flash light	Glass	9.6 μΩ cm	Abbel [18]
Silver	Flash light	PI	6.2 μΩ cm	Yung [19]
Silver	Flash light	PET	1.5 Ω/sq	Hosel [20]
Silver	Flash light	PET	4.9 μΩ cm	Kang [21]
Silver	Flash light	PET	0.95 Ω/sq	Chung [22]
Silver	Flash light	PI	–	Lee [13]
Silver	Flash light	PI	3.6 μΩ cm	Park [15]
Silver	Laser	Glass	–	Peng [23]
Copper	Flash light	PI	5 μΩ cm	Kim [24]
Copper	Flash light	PI	5 μΩ cm	Ryu [12]
Copper	Flash light	PI	173 μΩ cm	Han [25]
Copper	Flash light	PI	72 Ω/sq	Hwang [14]
Copper	Flash light	PET	388.3 μΩ cm	Wang [26]
Copper, Ni	Laser	–	–	Agarwala [27]
Copper, Sn, Ni	Laser	–	–	Khaing [28]

particle size distribution on the flash light sintering by comparing two nanoparticle systems (one with a uniform diameter of about 50 nm, the other with various particle diameters from 5 nm to 500 nm). In order to achieve high electrical conductivity in the sintered nickel nanoparticles, several flash light sintering parameters such as light energy and pulsed light patterns were optimized. Also, the nickel nanoink was optimized by changing the weight fractions of organic binder in the ink.

2. Experiments

Two types of nickel nanoparticles were used: QSI nickel nanoparticles (QNI, 99.9% > purity, Quantum Sphere Inc.) and Sigma-Aldrich nickel nanoparticles (SNI, 99.9% > purity, Sigma-Aldrich Co.). QSI nickel nanoparticles had a uniform diameter of about 50 nm, while Sigma-Aldrich nickel nanoparticles had various particle diameters ranging from 5 nm to 500 nm. The nickel nanoparticle ink was prepared as follows. First, 2.5 g of diethylene glycol (DEG, 99% > purity, Sigma-Aldrich Co.) and polyvinylpyrrolidone (PVP, wt.% 40,000, Sigma-Aldrich Co.) were mixed together under ultrasonication for 2 h. In order to study the influence of PVP on the flash light sintering, we varied the amount of PVP from 0.2 wt.% to 0.4 wt.% in the flash light sintering process. Second, 0.5 ml of N-dimethylformamide (99.8% purity, Sigma-Aldrich Co.) was added to a PVP/DEG solution under ultrasonication for 1 h. Finally, 2.0 g of nickel nanoparticles were added and dispersed in an ultrafast mixer (AJ300V, Ajintechnics) for 1 h. The viscosity of resulting nickel nanoink was in the range from 165 cSt to 350 cSt depending on the wt.% of PVP.

A polyimide (PI) film with a thickness of 225 μm was prepared as a substrate material and was ultrasonicated in ethanol and distilled water for 10 min to remove surface contamination. Nickel nanoparticle inks were coated onto the PI substrate using a spin coater (SC-200, Nanotech Co.) at 800 rpm for 30 s. The coated films were 2 cm × 2 cm. Once coated, the resulting films were thoroughly dried on a hot plate (HSD 180, MISUNG SCIENTIFIC Co.) at 150 °C for 20 min before flash light sintering. For the flash light generation, a xenon flash lamp (PerkinElmer Co.) was used. This lamp generates flash light via arc plasma generation with wavelengths ranging from 380 nm to 1.0 μm [12]. Manipulating the pulse number and intensity of the arc plasma enables control of the energy from 0.001 J/cm^2 to 100 J/cm^2. Transformations of the microstructure were observed by scanning electron microscopy (SEM, S4800, Hitachi, 15 kV operating voltage) and focused ion beam (FIB, LYRA FEG 1, TESCAN, 15 kV operating voltage), and conductivity was measured using a four-point probe method with a source meter (2015 THD, Keithley). Also, we conducted X-ray diffraction (XRD, D/MAX RINT 2000, Rigaku) using the Bragg–Brentano geometry with Cu Kα radiation to analyze the particle size and phases of materials. UV–vis (S-4100, Scinco) test were conducted to characterize the optical properties of the nickel nanoparticles, respectively. The samples of UV–vis test were prepared by 1–10 wt.% of nickel nanoparticles mixed with ethanol. The mixed solution with ethanol and nickel nanoparticle was treated with ultrasonication in 10 min to acquire the uniform dispersion of the nickel nanoparticles in ethanol.

Flash light sintering was divided into two-steps, preheating and the main sintering step, to acquire a fairly packed sintered film structure [15]. The preheating step was conducted to gradually remove the organic binder surrounding the nickel nanoparticles before the main sintering step (Fig. 1) [15]. Energy used for the preheating and the main sintering step was varied from 7.5 J/cm^2 to 17.5 J/cm^2. In the preheating step, 15 rectangular pulses (5 ms duration with a 30 ms pulse gap between pulses) were applied. On the other hand, a single pulsed light was irradiated in the main sintering step. The energy of the irradiated light was measured using a power meter (Nova II, People Laser Tech.).

3. Results and discussion

Fig. 2 shows the XRD patterns of the two types of dried nickel films. XRD patterns of all the nickel films exhibited diffraction peaks of the (111), (200), (220), and (311) planes of face-centered cubic nickel at 2θ values of 44.5°, 51.8°, 76.5°, and 92.9°, respectively [30–32]. However, the peaks of the nickel oxide were not observed in SNI and QNI films. Also, the peaks of the SNI film were sharper than those of the QNI film due to their mean size. Based on the peaks in the spectrum of each nickel film, the mean size of the nickel nanoparticles was calculated using Scherrer's formula as follows:

$$L = (0.9\lambda)/(B\cdot\cos\theta) \quad (1)$$

where L is the mean size of the alloy particles, λ is the X-ray wavelength (Cu Kα, λ = 0.1541 nm), θ is the maximum angle of the peaks, and B is the half-peak width for in radians. For accurate calculation, the Lorentzian fitting was conducted when the mean size of QNI nanoparticles was calculated due to the broadening of the XRD peaks of QNI nanoparticles. Meanwhile, the resolved Kα1 lines were used for calculating the mean size of SNI nanoparticles due to the very sharp XRD peaks of SNI nanoparticles. Thus, the mean size of QNI was calculated to be 7.16 ± 1.6 nm, and that of SNI was 35.45 ± 7.5 nm.

To determine the morphology of the nickel particles, SEM images were taken with (see inset Fig. 3). The SEM images show the spherical shape and size distribution of each type of nickel nanoparticles. The SEM image of dried QNI nanoparticles showed a regular size of about 50 nm (see inset figure in Fig. 3a). However, the SEM image of the dried SNI nanoparticles showed various diameters from 10 nm to 400 nm (see inset figure in Fig. 3b).

To quantify the size distribution for the types of nickel nanoparticles, we conducted a size distribution analysis using a size distribution analyzer (Scatteroscope I, K-ONE LTD). As shown in Fig. 3, the QNI nanoparticles showed a log-normal distribution with an average diameter of 52.4 nm. Meanwhile, the SNI nanoparticles showed three major diameter peaks at 8 nm, 50 nm and 200 nm. These results are similar to SEM images (insets in Fig. 3). From the relative particle number distribution, the relative weight fraction of the nanoparticles was calculated using the density of nickel and the volume a sphere as follows:

$$m = (4/3)\cdot\left(\rho\pi r^3\right). \quad (2)$$

The blue line in Fig. 3 is the relative weight fraction of nanoparticles with respect to their diameter. It is noteworthy that 0.01 wt.% of the nanoparticles with diameters smaller than 10 nm (34.27% in particle number portion) were present in the SNI nanoparticles. The discussion

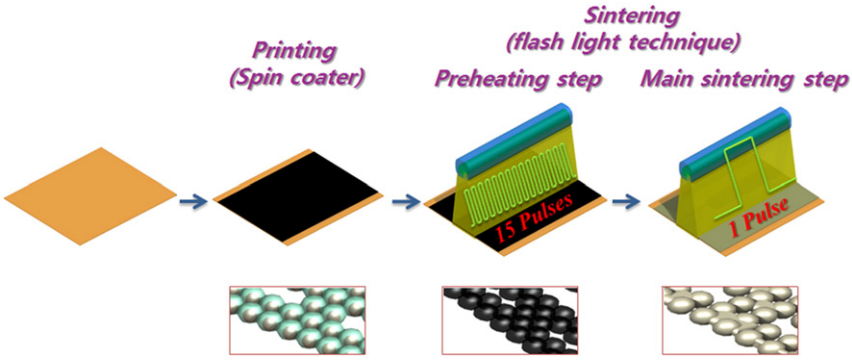

Fig. 1. The schematic of flash light sintering process.

of the critical role of the small size of nickel nanoparticles on the flash light sintering will be discussed later in this paper.

To find the optimum sintering conditions for the nickel nanoparticles, various experiments were conducted. First, we varied the PVP binder amount in the nickel nanoink, which retards the metal from oxidation and promotes dispersion of the nanoparticles [12]. As shown in Fig. 4, the weight fraction of PVP was varied from 0.2 to 0.4 wt.%, and sheet resistances were measured after the flash light sintering process. In this experiment, a one-step sintering process was used. Results show that sheet resistances decreased in all cases of SNI nanoparticles as the irradiated energy increased to 14.5 J/cm^2 (Fig. 4). If the irradiated light energy was higher than 15.5 J/cm^2, the SNI nanoparticles were burned, and the sheet resistance increased again. Among the samples tested, the 0.25 wt.% PVP/Ni nanoparticle ink showed the lowest sheet resistance. The SEM images in Fig. 5 show different morphologies of SNI nanoparticles with respect to PVP wt.% after flash light sintering. In the 0.4 wt.% PVP case, a good amount of organic binder still remained after 14.5 J/cm^2 of flash light energy irradiation (Fig. 5a). In the case of 0.35 wt.% PVP, small connections could be found, and some amount of PVP remained (Fig. 5b). The 0.3 wt.% and 0.25 wt.% PVP cases show a clear SEM image of heavily agglomerated SNI nanoparticles without any remaining organic binders (Fig. 5c, d). Those cases also showed denser necking connections among the nanoparticles as the wt.% of nickel nanoparticle decreases. However, the 0.2 wt.% PVP case shows few necking connections among the nanoparticles. This might be because the 0.2 wt.% PVP is too small to bind the nanoparticles; thereby, all of the PVP may evaporate before the necking junctions can form during the flash light irradiation (Fig. 5e). Therefore, in this work, 0.25 wt.% PVP was used in the nickel nanoink for further optimizing the flash light process due to its the lowest sheet resistance and denser necking connections among the nanoparticles. However, in the case of QNI nanoparticles, the flash light sintered nanoparticles showed a very high sheet resistance greater than 500 Ω/sq regardless of the energy and PVP ratio (see Fig. 4). The reason for the poor sintering quality of QNI nanoparticles will be discussed below (Fig. 5f).

Second, we optimized the two-step sintering process composed of 15 multi-pulsed preheating irradiations followed by a single pulsed sintering step (see Fig. 1) by varying the light energies in each steps [15]. As shown in Fig. 6, the sheet resistance of SNI nanoparticles decreased as the main sintering energy was increased up to 17.5 J/cm^2. The 12.5 J/cm^2 preheated case showed the lowest sheet resistance for main sintering step energies (see Fig. 6). It was found that the higher preheating energy case is favorable for obtaining good conductivity. Fig. 7a and b shows the SEM images of the sintered SNI films with

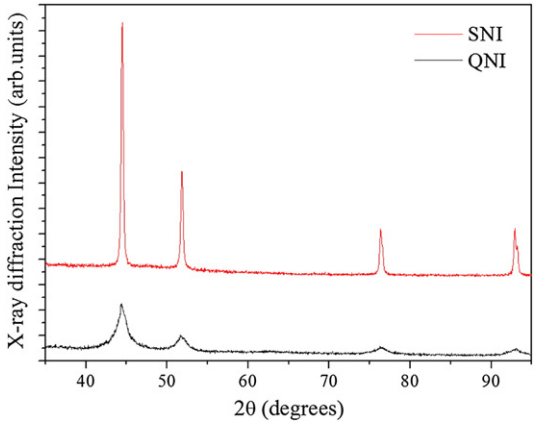

Fig. 2. XRD images of each nickel nanoparticles.

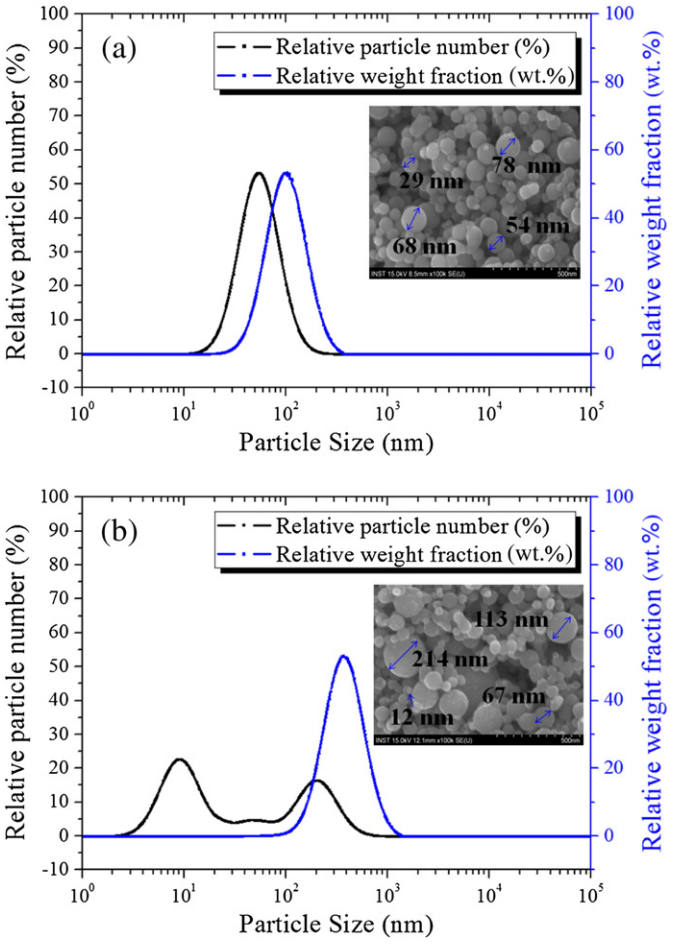

Fig. 3. The size distribution results and SEM images of each nickel nanoparticles; (a) QNI and (b) SNI.

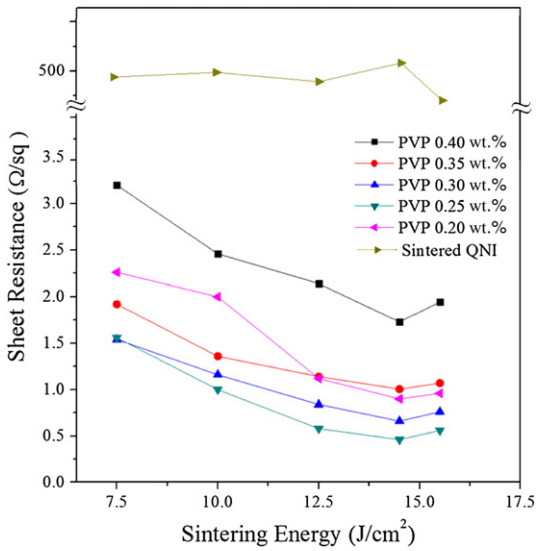

Fig. 4. Electrical sheet resistance of the flash light sintered SNI nanofilms as changing irradiation energy and the weight ratio of PVP (SNI nanoparticle amount: 2.0 g, pulse number: 1) and QNI nanofilms.

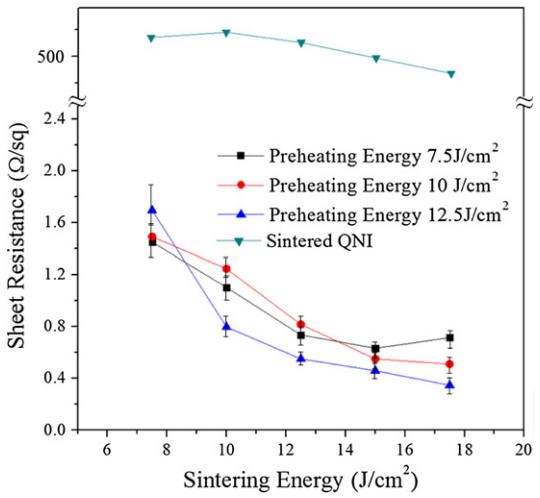

Fig. 6. Electrical sheet resistance of the flash light sintered SNI and QNI nanofilms as changing irradiation energy.

different preheating energies (7.5 J/cm^2 and 12.5 J/cm^2, respectively) followed by a 17.5 J/cm^2 main sintering step. As shown in SEM images, the 12.5 J/cm^2 preheated SNI films (Fig. 7b) had a more densely connected necking structure than the 7.5 J/cm^2 preheated case (Fig. 7a) after a 17.5 J/cm^2 main sintering step. If we applied an energy greater than 17.5 J/cm^2 as the main sintering energy, the SNI and QNI films were burned out, cracks occurred on the surface, and the sheet resistance became too high or infinite (Fig. 7c).

Based on the results, the 12.5 J/cm^2 preheating–17.5 J/cm^2 main sintering energy flash light process was determined as the optimum for SNI nanoparticles. With the optimized two-step flash light sintering

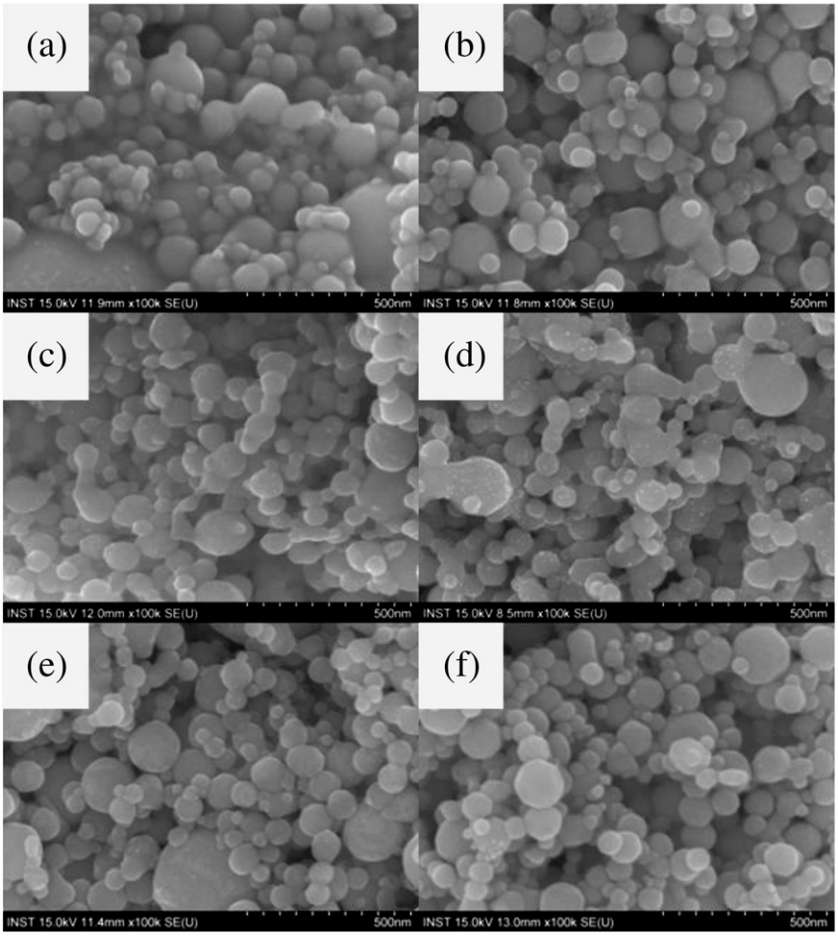

Fig. 5. The SEM images of the flash light sintered SNI nanofilms as changing the weight ratio of PVP: (a) PVP 0.4 wt.%, (b) PVP 0.35 wt.%, (c) PVP 0.3 wt.%, (d) PVP 0.25 wt.%, (e) PVP 0.2 wt.% and (f) QNI nanofilms with the weight ratio of PVP 0.2 wt.% (irradiated flash light energy: 14.5 J/cm^2, SNI nanoparticle amount: 2.0 g, irradiation energy: 14.5 J/cm^2, pulse number: 1).

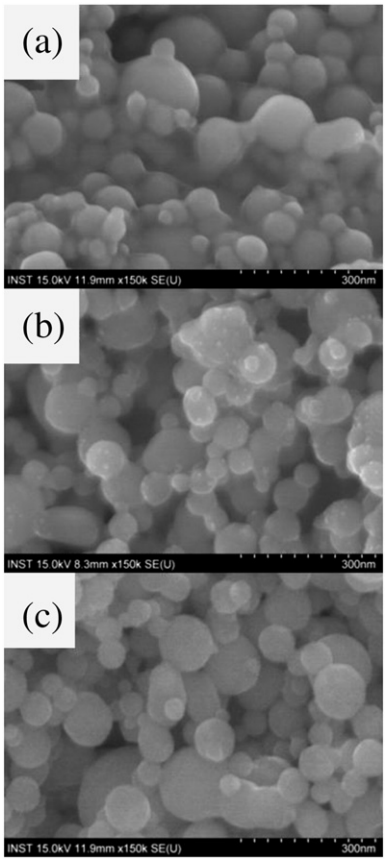

Fig. 7. SEM images of the flash light sintered SNI nanofilms as changing irradiation energy (SNI nanoparticle amount: 2.0 g, DEG amount: 2.5 g, PVP amount: 0.2 wt.% in all cases); (a) 7.5 J/cm^2 preheated–17.5 J/cm^2 sintered, and (b) 12.5 J/cm^2 preheated–17.5 J/cm^2 sintered, and (c) 12.5 J/cm^2 preheated–17.5 J/cm^2 sintered QNI nanofilms.

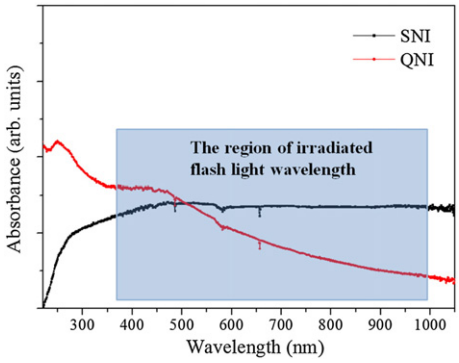

Fig. 9. Normalized extinction spectra of QNI and SNI nanoparticle systems.

process, a sheet resistance of 0.347 Ω/sq was obtained for the SNI film, which is suitable for MLCCs and printed electronics [1–5,10–13]. To calculate the resistivity of the SNI films, we took the FIB image as shown in Fig. 8. As the results, the thickness of the nickel film was changed from about 4.5 μm to 2.2 μm in the optimum flash light sintering condition (Fig. 8a, b). Thus, the resistivity of the SNI film was calculated to be 76.34 μΩ cm. However, in the QNI nanoparticle case, only high sheet resistances of about 500 Ω/sq, i.e., 1000 times higher than that of the SNI film, were obtained under any flash light sintering conditions. To determine why SNI films could be sintered while QNI films could not, we focused on the size effects of the nanoparticles. Basically, as the nanoparticle sizes change, their optical and thermal properties change [6–9,33–37]. In order to investigate the effect of size distribution of nickel nanoparticles on the flash light absorption, we conducted UV–vis experiments with wavelength ranges from 200 nm to 1.1 μm. Fig. 9 shows the light absorption for each type of nanoparticle. In the case of QNI nanoparticles, an absorbing peak at about 250 nm was shown, and it gradually decreased as the wavelength increased. The 250 nm absorbing peak of the 50-nm-diameter nickel nanoparticles agreed with the results of Hillenbrand et al. [35]. However, in the case of SNI nanoparticles, a broad range of light was absorbed because 50 nm and 200 nm diameter nanoparticles have a broad plasmonic resonance peak in the range of 200 nm–1.1 μm wavelength. According to Hillenbrand et al., 60-nm-diameter nickel nanoparticles have resonance absorbing wavelength peaks from 200 nm to 650 nm, while 200-nm-diameter particles have resonance peaks from 650 nm to 1.0 μm [35]. These different light resonance peaks with different nanoparticle diameters show a broad range absorption of light to the SNI nanoparticles (Fig. 9). Note that our flash light generated broad range white light with wavelengths ranging from 380 nm to 1.0 μm (Fig. 10) [12]. It is also noteworthy that the wavelength range of the white flash light is coincident with the absorption range of SNI nanoparticles (see blue window in Fig. 9). Therefore, it can be deduced that SNI nanoparticles can more efficiently absorb the whole wavelength range of the irradiated flash light from the xenon lamp than can the QNI nanoparticles.

Another factor affecting the flash light sintering of nanoparticles is their melting temperature. The theoretical melting temperature of nickel

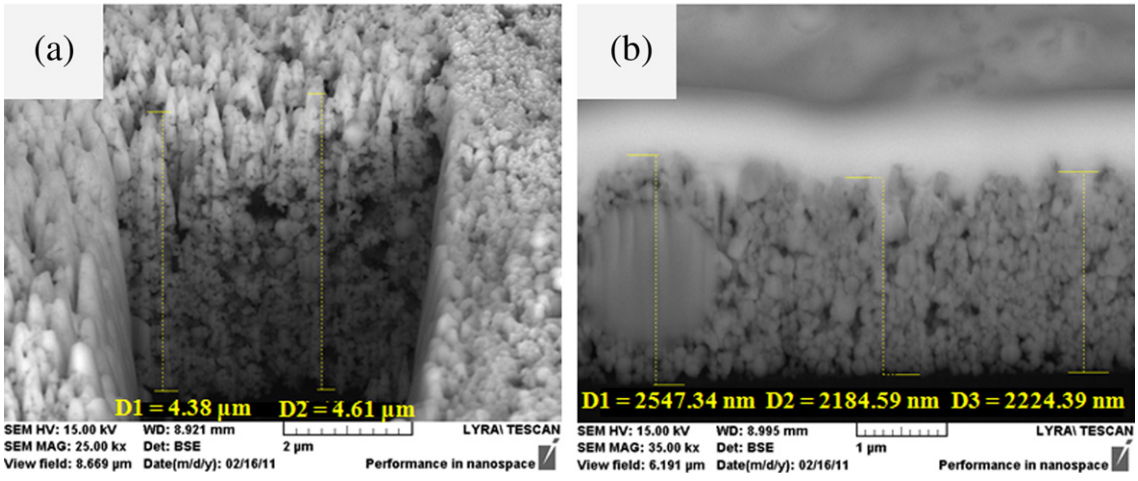

Fig. 8. FIB images of the: (a) dried SNI film and (b) 12.5 J/cm^2 preheated–17.5 J/cm^2 sintered SNI films.

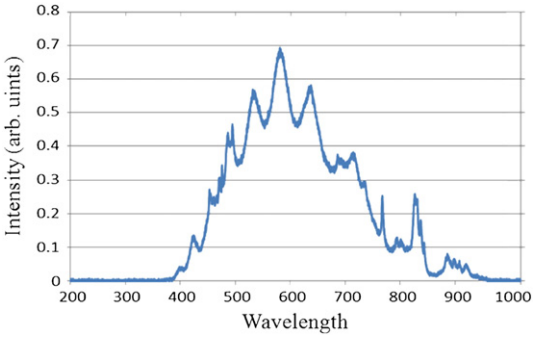

Fig. 10. The wavelength spectra of the flash light.

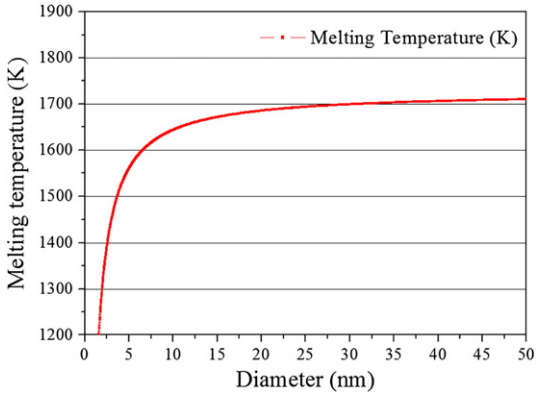

Fig. 11. The predicted melting temperature of nickel nanoparticles changing with particle size.

nanoparticles varies with the diameter of the nanoparticles according to the following equation [24,37]:

$$T_m = T_0\left(1-(4/\rho_s Ld)\left[\gamma_s-\gamma_l\left(\rho_s/\rho_l\right)^{2/3}\right]\right) \quad (3)$$

where T_m is the melting temperature of the metal nanoparticles, T_0 is the melting temperature of the bulk metal, ρ_s is the density of the metal in the solid state, ρ_l is the density of the metal in the liquid state, γ_s is the surface tension of the metal in the solid state, γ_l is the surface tension of the metal in the liquid state, L is the latent heat of fusion, and d is the diameter of the metal nanoparticle. The material constants of nickel are shown in Table 2. Eq. (3) predicts that the melting temperature of nickel is significantly depressed when the particle diameter is smaller than 10 nm, as shown in Fig. 11.

Based on the results of size distribution analysis (see Fig. 3), it was found that about 0.01 wt.% of SNI nanoparticles were smaller than 10 nm, while almost the QNI nanoparticles were larger than 10 nm. The 0.01 wt.% of the nanoparticles with diameters smaller than 10 nm in SNI nanoparticles, which correspond to 34.27% in particle number portion, might play a crucial role in flash light sintering, as they could easily melt due to their low melting temperature. Therefore, these small nanoparticles could connect the larger surrounding nanoparticles more easily during flash light irradiation. Also, these small particles would fill the voids between large particles, which results in tight packing of nanoparticles in sintered layer. Based on the discussion above, we conclude that there is a synergetic effect of optical and thermal properties of diverse size nanoparticles in SNI nanoparticles that provide a fairly good sintered film after flash light irradiation. Again, it is noteworthy that 0.01 wt.% of the nanoparticles (34.3% in particle number portion) with diameters smaller than 10 nm in the SNI nanoink enabled the flash light sintering process even though the mean particle size (35.45 ± 7.5 nm) was larger than that of QNI (7.16 ± 1.6 nm). This gives us an important guideline for low price nanoink fabrication suitable for flash light sintering as the manufacturing price of nanoparticles becomes quite expensive for particle sizes smaller than about 30 nm.

Additionally, to show the applicability of Ni nanoink and flash light sintering techniques for large area electrode patterning on various substrates, we printed the nickel patterns via a screen printing method using SNI nickel ink. The viscosity of the nickel nanoink was adjusted by mixing ethanol suitable for screen printing. The length of simple line pattern was 8 cm and the diameter of the university mark (Hanyang University) was 6 cm as shown in Fig. 12. The flash light sintering conditions were optimal conditions (the 12.5 J/cm^2 preheating–17.5 J/cm^2 main sintering energy). As the results, the printed nickel patterns were sintered with good conductivity regardless of the substrate type (on the polyimide film; Fig. 12a, b, e and on the photo paper; Fig. 12c, d, f).

Also, the research is currently underway to determine the optimal particle size distribution combined with nano-size and micro-size particles to minimize the manufacturing cost of the nanoink.

Table 2
Physical constants of nickel.

	Solid	Liquid
Specific gravity, ρ (kg/m^3)	8908	7810
Surface tension, γ (J/m^2)	0.222	0.1687
Latent heat of fusion, L (J/kg)	2.98×10^5	–

T_0: The melting temperature of bulk nickel (1728 K).

4. Conclusion

In this work, we analyzed the size effect for the sintering of nickel nanoparticles with two types of nickel nanoparticle systems: one with a uniform diameter of about 50 nm and another with various particle diameters from 5 nm to 500 nm. In this study, the nickel nanoparticles with various sizes were sintered using the optimized weight fraction of the PVP binder in the ink and the optimized two-step flash light sintering process. The resistivity of the optimally sintered SNI film was

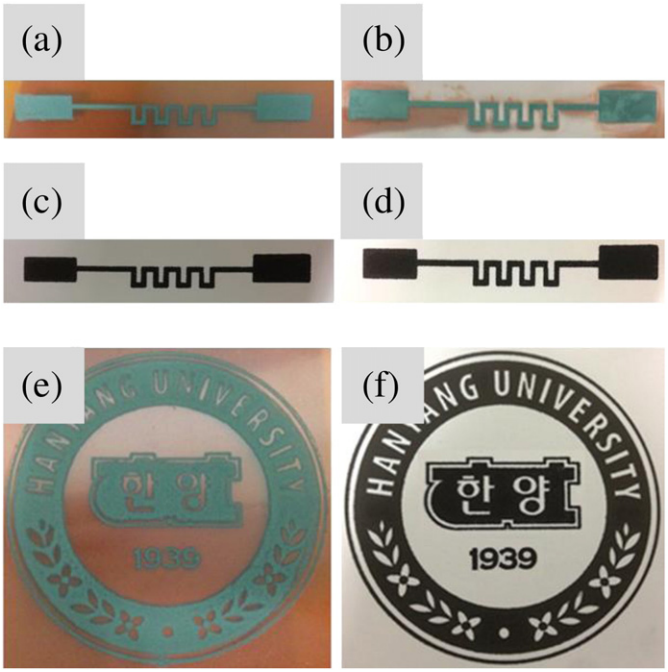

Fig. 12. The photograph of the printed nickel films using the screen printing method; simple line pattern: (a) before sintering, (b) after sintering on the PI film and (c) before sintering, (d) after sintering on the paper, and sintered Hanyang mark pattern: (e) on the PI film and (f) the paper.

76.34 μΩ cm, which is low enough to be used in MLCC electrodes and printed electronics.

Acknowledgments

This work was supported by the Basic Science Research Program through the National Research Foundation of Korea (NRF) funded by the Ministry of Education (Nos. 2010-0007120, 2012R1A6A1029029 and 2013M2A2A9043280).

References

[1] H. Kishi, Y. Mizuno, H. Chazono, Jpn. J. Appl. Phys. 42 (2003) 1.
[2] J.Y. Lee, J.H. Lee, S.H. Hong, Y.K. Lee, J.Y. Choi, Adv. Mater. 15 (2003) 1655.
[3] D.F.K. Hennings, J. Eur. Ceram. Soc. 21 (2001) 1637.
[4] J. Yamamatsu, N. Kawano, T. Arashi, A. Sato, Y. Nakano, T. Nomura, J. Power Sources 60 (1996) 199.
[5] D.H. Im, S.H. Hyun, S.Y. Park, B.Y. Lee, Y.H. Kim, J. Mater. Sci. 41 (2006) 6425.
[6] Z. Libor, Q. Zhang, Mater. Chem. Phys. 114 (2009) 902.
[7] Z. Liu, S. Li, Y. Yang, S. Peng, Z. Hu, Y. Qian, Adv. Mater. 15 (2003) 1946.
[8] Y. Hou, S. Gao, J. Mater. Chem. 13 (2003) 1510.
[9] H.T. Zhang, G. Wu, X.H. Chen, X.G. Qiu, Mater. Res. Bull. 41 (2006) 495.
[10] D. Li, D. Sutton, A. Burgess, D. Graham, P.D. Calvert, J. Mater. Chem. 19 (2009) 3719.
[11] J. Perelaer, P.J. Smith, D. Mager, D. Soltman, S.K. Volkman, V. Subramanian, J.G. Korvink, U.S. Schubert, J. Mater. Chem. 20 (2010) 8446.
[12] J. Ryu, H.S. Kim, H.T. Hahn, J. Electron. Mater. 40 (2011) 42.
[13] D.J. Lee, S.H. Park, S. Jang, H.S. Kim, Jehoon Oh, Y.W. Song, J. Micromech. Microeng. 21 (2011) 125023.
[14] H.J. Hwang, W.H. Chung, H.S. Kim, Nanotechnology 23 (2012) 485205.
[15] S.H. Park, S. Jang, D.J. Lee, J.H. Oh, H.S. Kim, J. Micromech. Microeng. 22 (2012) 015013.
[16] D. Tobjörk, H. Aarnio, P. Pulkkinen, R. Bollström, A. Määttänen, P. Ihalainen, T. Mäkelä, J. Peltonen, M. Toivakka, H. Tenhu, R. Österbacka, Thin Solid Films 520 (2012) 2949.
[17] Y. Galagan, E.W.C. Coenen, R. Abbbel, T.J. van Lammeren, S. Sabik, M. Barink, E.R. Meinders, R. Andriessen, P.W.M. Blom, Org. Electron. 14 (2013) 38.
[18] R. Abbel, T. van Lammeren, R. Hendriks, J. Ploegmakers, E.J. Rubingh, E.R. Meinders, W.A. Groen, MRS Commun. 2 (2012) 145.
[19] K.C. Yung, X. Gu, C.P. Lee, H.S. Choy, J. Mater. Process. Technol. 210 (2010) 2268.
[20] M. Hosel, F.C. Krebs, J. Mater. Chem. 22 (2012) 15683.
[21] J.S. Kang, J. Ryu, H.S. Kim, H.T. Hahn, J. Electron. Mater. 40 (2011) 2268.
[22] W.H. Chung, H.J. Hwang, S.H. Lee, H.S. Kim, Nanotechnology 24 (2013) 035202.
[23] P. Peng, A. Hu, Y. Zhou, Appl. Phys. A 108 (2012) 685.
[24] H.S. Kim, S.R. Dhage, D.E. Shim, H.T. Hahn, Appl. Phys. A 97 (2009) 791.
[25] W.S. Han, J.M. Hong, H.S. Kim, Y.W. Song, Nanotechnology 22 (2011) 395705.
[26] B.Y. Wang, T.H. Yoo, Y.W. Song, D.S. Lim, Y.J. Oh, ACS Appl. Mater. Interfaces 5 (2013) 4113.
[27] M. Agarwala, D. Bourell, J. Beaman, H. Marcus, J. Barlow, Rapid Prototyp. J. 1 (1995) 26.
[28] M.W. Khaing, J.Y.H. Fuh, L. Lu, J. Mater. Process. Technol. 113 (2001) 269.
[29] R. Karmhag, G.A. Niklasson, M. Nygren, J. Appl. Phys. 89 (2001) 3012.
[30] Y.D. Li, L.Q. Li, H.W. Liao, H.R. Wang, J. Mater. Chem. 9 (1999) 2675.
[31] E.M.A. Jamal, P.A. Joy, P. Kurian, M.R. Anantharaman, Polym. Bull. 64 (2010) 907.
[32] Y. Gao, J. Zhao, B. Zhou, Y. Zhu, Z. Wang, Colloids Surf. A 368 (2010) 137.
[33] C.L. Haynes, R.P. Van Duyne, J. Phys. Chem. 105 (2001) 5599.
[34] K.C. Lee, S.J. Lin, C.H. Lin, C.S. Tsai, Y.J. Lu, Surf. Coat. Technol. 202 (2008) 5339.
[35] J. Chen, P. Albella, Z. Pirzadeh, P.A. Gonzalez, F. Huth, S. Bonetti, V. Bonanni, J. Akerman, J. Nogues, P. Vavassori, A. Dmitriev, J. Aizpurua, R. Hillenbrand, Small 7 (2011) 2341.
[36] G.W. Bryant, F.J.G. de Abajo, J. Aizpurua, Nano Lett. 8 (2008) 631.
[37] P. Buffat, J.P. Borel, Phys. Rev. A 13 (1976) 2287.